



ELSEVIER

Available online at www.sciencedirect.com

Journal of Hydrodynamics

2014, 26(3):351-362
DOI: 10.1016/S1001-6058(14)60040-8[www.sciencedirect.com/
science/journal/10016058](http://www.sciencedirect.com/science/journal/10016058)

Scaling of maximum probability density function of velocity increments in turbulent Rayleigh-Bénard convection*

QIU Xiang (邱翔)

School of Science, Shanghai Institute of Technology, Shanghai 200235, China, E-mail: emqiu@163.com

HUANG Yong-xiang (黄永祥), ZHOU Quan (周全)

Shanghai Institute of Applied Mathematics and Mechanics, Shanghai University, Shanghai 200072, China

SUN Chao (孙超)

Physics of Fluids Group, University of Twente, AE Enschede, The Netherlands

(Received March 31, 2014, Revised May 16, 2014)

Abstract: In this paper, we apply a scaling analysis of the maximum of the probability density function (pdf) of velocity increments, i.e., $p_{\max}(\tau) = \max_{\Delta u_\tau} p(\Delta u_\tau) \sim \tau^{-\alpha}$, for a velocity field of turbulent Rayleigh-Bénard convection obtained at the Taylor-microscale Reynolds number $Re_\lambda \approx 60$. The scaling exponent α is comparable with that of the first-order velocity structure function, $\zeta(1)$, in which the large-scale effect might be constrained, showing the background fluctuations of the velocity field. It is found that the integral time $T(x/D)$ scales as $T(x/D) \sim (x/D)^{-\beta}$, with a scaling exponent $\beta = 0.25 \pm 0.01$, suggesting the large-scale inhomogeneity of the flow. Moreover, the pdf scaling exponent $\alpha(x, z)$ is strongly inhomogeneous in the x (horizontal) direction. The vertical-direction-averaged pdf scaling exponent $\tilde{\alpha}(x)$ obeys a logarithm law with respect to x , the distance from the cell sidewall, with a scaling exponent $\xi \approx 0.22$ within the velocity boundary layer and $\xi \approx 0.28$ near the cell sidewall. In the cell's central region, $\alpha(x, z)$ fluctuates around 0.37, which agrees well with $\zeta(1)$ obtained in high-Reynolds-number turbulent flows, implying the same intermittent correction. Moreover, the length of the inertial range represented in decade $\tilde{T}_I(x)$ is found to be linearly increasing with the wall distance x with an exponent 0.65 ± 0.05 .

Key words: Rayleigh-Bénard convection, scaling, probability density function (pdf)

Introduction

The small-scale fluctuations of turbulent velocity or temperature fields are believed to be universal for high-Reynolds-number turbulent flows^[1]. This has

been recognized as a milestone progress in the turbulence research, known as Kolmogorov 1941 (K41) theory^[2]. To characterize this universality, the q th-order structure-functions (SFs) are defined as

$$S_q(r) = \left\langle |u(x+r) - u(x)|^q \right\rangle \sim r^{\zeta(q)} \quad (1)$$

where r is the spatial separation and lies in the so-called inertial range, and $\zeta(q) = q/3$ for the K41 theory^[2]. The above scaling relation has been examined in many different types of turbulent flows by applying the concept of multifractal.^[3-6] Besides the SFs analysis, several methodologies have also been proposed, e.g., wavelet-based methods^[7-9], Hilbert-based method^[10-12], scaling analysis of probability density

* Project supported by the Natural Science Foundation of China (Grant Nos. 11102114, 11202122 and 11222222), the Innovation Program of Shanghai Municipal Education Commission (Grant No. 13YZ008, 13YZ124), the Shanghai Shuguang Project (Grant No. 13SG40), and the Program for New Century Excellent Talents in University (Grant No. NCET-13-0).

Biography: QIU Xiang (1978-), Male, Ph. D., Associate Professor

Corresponding author: ZHOU Quan,
E-mail: qzhou@shu.edu.cn

function (pdf)^[13], etc., to quote a few. Note that each method has its own advantages and limitations. For example, due to the nonlocal property of the SFs, it is strongly influenced by large-scale structures, known as infrared (IR) effect, or by energetic structures (e.g., ramp-cliff structure in passive scalar, seasonal forcing in environment data, etc.)^[11,14-17], and, however, the wavelet-based (resp. Fourier-based) methods may suffer from higher-order harmonic problem, etc.^[11,12,18].

Specifically, for the Rayleigh-Bénard (RB) convection system, buoyant forces are relevant. The flow is then driven by buoyant forces mainly via the so-called thermal plumes^[6,19-21]. According to Bolgiano and Obukhov's arguments, above the so-called Bolgiano length scale l_B (see the definition below), instead of the K41 scaling $S_q(r) \sim r^{q/3}$, the Bolgiano-Obukhov (BO59) scaling $S_q(r) \sim r^{3q/5}$ is expected, at least for the vertical velocity^[6,19,20]. Based on the direct spatial velocity measurements using the particle image velocimetry (PIV) technique, Sun et al.^[22] found a K41-like scaling with intermittent corrections at the cell, while near the sidewall where thermal plumes abound, vertical velocity (longitudinal direction) and temperature were found to exhibit a different scaling. However, the horizontal velocity is still similar to a K41-like scaling with intermittent corrections, as the influence of the thermal plumes on the horizontal direction is much less than that of the vertical one^[22]. For the temperature fluctuations near the cell sidewall, Huang et al.^[13] found a K41-like (resp. Kolmogorov-Obukhov-Corrsin, KOC for short) scaling behavior in the probability space, i.e., $p_{\max}(\tau) = \max_{\Delta\theta_\tau} p(\Delta\theta_\tau) \sim \tau^{-\alpha}$, where $\Delta\theta_\tau = \theta(t+\tau) - \theta(t)$ and τ is the temporal separation. However, near the cell sidewall where thermal plumes are abundant, the BO59 scaling is expected^[6]. They therefore argued that the temperature fluctuations might be considered as a K41-like background fluctuations superposed by thermal plumes (BO59-like structures). For the small-scale statistics in turbulent RB convection, we refer to the reader to the very nice review paper by Lohse and Xia^[6].

In this paper, we generalize the idea of pdf scaling to the velocity field measured in a cylindrical turbulent RB convection cell. We first show that the flow is inhomogeneous. It is further found that the integral time scale T has a power law relation with the wall distance x , i.e., $T \sim (x/D)^{-\xi}$, with a scaling exponent $\xi = 0.25$, where D is the diameter of the cell. Due to the spatial inhomogeneity of the RB flows, we study the pdf scaling in temporal domain. A more than one decade inertial range is observed, which is larger than the one in spatial domain^[22]. We find that the

scaling exponent $(x/D, z)$ depends on x/D , the distance from the sidewall. A logarithmic law, i.e. $\tilde{\alpha}(x/D) \sim \gamma \lg_{10}(x/D)$, with scaling exponent $\gamma = 0.22$ is found within the velocity boundary layer and $\gamma = 0.28$ from near the cell sidewall to the cell's central region. Moreover, a power law behavior is found for the length of the inertial range with a scaling exponent 0.69 ± 0.05 . Finally, for comparison, the SFs analysis is also performed in temporal domain. Except for the details, the SFs results consist with the pdf scaling results.

1. Scaling behavior of maximum probability density function of velocity increments

More recently, Huang et al.^[13] discovered a scaling property of the increment's pdfs (we work in temporal domain), i.e.,

$$p_{\max}(\tau) \sim \tau^{-\alpha} \quad (2)$$

where p_{\max} is the maximum value of the pdf $p_{\max} = \max_{\Delta X_\tau} p_\tau(\Delta X_\tau)$ of increments $\Delta X_\tau(t) = X(t+\tau) - X(t)$. Here α is the scaling exponent in probability space and is comparable with the scaling exponent of first-order SF $\zeta(1)$, at least for H -self-similarity processes.^[13] When the pdf scaling approach was applied to the temperature obtained in the near sidewall region of a cylindrical RB convection cell, instead of the BO59 scaling $\zeta_\theta(1) = 1/5$, a KOC-like scaling behavior with $\alpha_\theta \approx 0.33$ was obtained^[13]. However, the direct estimation of the first-order SF provides $\zeta_\theta(1) = 0.19$, a value preferable to the BO59 scaling. It has been shown experimentally that the maximum pdf $p_{\max}(\tau)$ counts a 'real' background fluctuation since the location of the $p_{\max}(\tau)$ is always around $\Delta X_\tau \approx 0$ ^[13]. Therefore, the obtained KOC-like scaling has been interpreted as that, at least in the near sidewall region, the temperature fluctuation can be understood as KOC-like background fluctuation superposed with buoyant structures, such as thermal plumes^[13].

We briefly recall the approach we used in this study. As shown in Huang et al.^[13], the pdf scaling $p_{\max}(\tau)$ can be analytically derived for fractional Brownian motions and H -self-similarity processes in the probability space. Here we obtain the scaling relation Eq.(2) for velocity increments by a dimensional consideration. Taking a turbulent velocity time series $u(t)$, the velocity increment is defined as, i.e.,

$$\Delta X_\tau(t) = \Delta u_\tau(t) = u(t+\tau) - u(t) \quad (3)$$

One can define a pdf $p_\tau(\Delta X_\tau)$ of $\Delta X_\tau(t)$ for a given separation time τ . Note that the probability $p_\tau(\Delta X_\tau)$ of $\Delta X_\tau(t)$ is a pure number without dimension. Thus one has

$$[p_\tau(\Delta X_\tau)] = [\Delta X_\tau]^{-1} = [u]^{-1} \quad (4)$$

where $[\cdot]$ means dimension. According to Kolmogorov's similarity hypotheses^[1,2], we expect the following power law

$$p_\tau(\Delta X_\tau) = \Delta X_\tau^{-1} \sim \tau^{-\alpha} \quad (5)$$

where α is comparable with the first-order SF scaling exponent $\zeta(1)$ and is to be $1/3$ for the Kolmogorov nonintermittent value for homogeneous and isotropic turbulent flows^[11,13]. However, the above Eq.(5) may not hold for the whole pdf $p_\tau(\Delta X_\tau)$. Inspired by a skeleton scaling of pdf found by Huang et al.^[10], Huang et al.^[13] proposed the maximum pdf $\max_{\Delta X_\tau} \{p_\tau(\Delta X_\tau)\}$ at a given scale as a surrogate of the whole pdf $p_\tau(\Delta X_\tau)$, i.e.,

$$p_{\max}(\tau) = \max_{\Delta X_\tau} \{p_\tau(\Delta X_\tau)\} \sim \tau^{-\alpha} \quad (6)$$

As was mentioned above, the scaling exponent α is comparable with the first-order SF scaling exponent $\zeta(1)$ ^[13]. Experimentally, the maximum pdf of the increment $p_\tau(\Delta X_\tau)$ is usually taken around $\Delta X_\tau \approx 0$. Therefore, it has been interpreted as background fluctuations of the velocity or temperature fields, in which the effect of large scale structures, e.g., thermal plumes in the RB system, is excluded^[13]. More details of the present pdf scaling method can be found in Refs.[11,13].

In this study, we extend the pdf scaling analysis to the horizontal velocity obtained in turbulent RB system by using PIV technique. However, due to the spatial inhomogeneity of the flow (see next section for detail), we consider the approach in the temporal domain. The empirical pdf is estimated as

$$p(\Delta X_\tau) = \frac{N_i}{Nd\hbar} \quad (7)$$

where N_i is the number of events in the i th bin, N the total length of the data, and $d\hbar$ the width of bins. It is found empirically that the pdf $p_\tau(\Delta X_\tau)$, the maximum pdf $p_{\max}(\tau)$ and the corresponding power law Eq.(6) are almost independent with the range of bin width $d\hbar$ ^[13]. Empirically, it is found when the data

length $L \geq 10^5$ (in data points) the error between estimated and given Hurst number is less than 1% see more discussion in Section 2. To ensure a good statistics, we perform in this study a box-counting method to estimate the empirical pdf with data length $L \geq 10^5$.

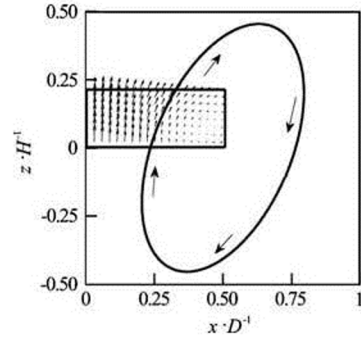


Fig.1 Illustration of the PIV measurement area in x - z plane $0 < x/D < 0.5$ and $0 < z/H < 0.21$. The time averaged velocity vector $\mathbf{U}(x, z)$ is illustrated by arrows. Note that the flow is inhomogeneous in both x - and z -directions. The so-called large-scale circulation is illustrated by an ellipse and arrow. The inset shows the cylindrical geometry of the convection cell

2. Experimental data and inhomogeneity of Rayleigh-Bénard flows

2.1 Rayleigh-Bénard convection experiment

The convection cell has been described in detail elsewhere^[22,23]. Briefly it is a vertical cylinder with top and bottom copper plates and Plexiglas sidewall. The height and the inner diameter of the cell are 0.193 m and 0.19 m, respectively, and thus the aspect ratio is $\Gamma \equiv D/H \approx 1$. The velocity field was measured by using the particle image velocimetry (PIV) technique. A square-shaped jacket made of flat glass plates and filled with water is fitted round the sidewall, which greatly reduced the distortion effect to the PIV images caused by the curvature of the cylindrical sidewall. The measurements were made from near the cell sidewall to the cell center (see Fig.1). The Prandtl number and Rayleigh number are respectively $Pr \equiv \nu/\kappa = 4.3$ and $Ra \equiv \beta g \Delta H^3 / \nu \kappa = 7 \times 10^9$ with g being the gravitational acceleration, Δ the temperature difference across the fluid layer, and β , ν and κ being, respectively, the thermal expansion coefficient, the kinematic viscosity, and the thermal diffusivity of the working fluid (water). The corresponding integral Reynolds number $Re \equiv WH/\nu \approx 3,600$, where W is the maximal vertical velocity near the sidewall, and the associated Reynolds number based on the Taylor microscale is of the order of $Re_\lambda \propto \sqrt{Re} \approx$

$60^{[24]}$. During the experiment the convection cell was placed inside a thermostat box, which was kept at the mean temperature of the working fluid (40°C), and was tilted by a small angle of $\sim 0.5^{\circ}$ so that the velocity measurements were made within the vertical plane of the large-scale circulation (LSC) and at the mid-height of the cell. In each measurement, the measuring region has an area $\Delta x \times \Delta z$ of $0.00052 \times 0.00041 \text{ m}^2$ with a spatial resolution of 0.00066 m , corresponding to 79×63 measured velocity vectors, see Fig.1 and discussion for inhomogeneity below. Polyamide spheres of $50 \mu\text{m}$ in diameter and $1.03 \times 10^3 \text{ kg/m}^3$ density were used as seed particles and the laser light-sheet thickness is $\sim 0.0005 \text{ m}$. The measurements lasted 1 h, corresponding to an acquisition time of around 120 turnover times of the large-scale circulation. A total of 7 500 vector maps were acquired with sampling frequency $\sim 2 \text{ Hz}$. Denote the laser-illuminated plane as the xz plane, the horizontal velocity component $u(x, z)$ and the vertical component $w(x, z)$ were then obtained. The uncertainty of PIV measurements is about 1%, which is too small to impact the results presented below.

The global Bolgiano length scale, the Kolmogorov length scale and the Taylor microscale are

$$L_B = \frac{HNu^{1/2}}{(RaPr)^{1/4}}, \quad \eta = \frac{HPr^{1/2}}{(RaNu)^{1/4}}, \quad \lambda = \left(\frac{15\nu\sigma_u^2}{\varepsilon} \right)^{1/2} \quad (8)$$

where H is the height of the cell, Nu the Nusselt number, σ_u the maximum value of the u_{rms} , and ε the mean energy dissipation rate, which can be estimated as follows^[25]

$$\varepsilon = \frac{\nu^3}{H^4} (Nu - 1) Ra Pr^{-2} \quad (9)$$

For the present data, we have $L_B \approx 0.005 \text{ m}$, and $\eta \approx 0.0004 \text{ m}$ and $\lambda \approx 0.008 \text{ m}$ ^[22]. The corresponding global Bolgiano time scale and the Kolmogorov time scale are respectively

$$\tau_B = \frac{\tau_0 Nu^{1/2}}{(RaPr)^{1/4}}, \quad \tau_\eta = \frac{\tau_0 Pr^{1/2}}{(RaNu)^{1/4}} \quad (10)$$

where τ_0 is the turnover time (resp. the period large-scale circulation), which is estimated by using the autocorrelation function of the velocity in the near sidewall region. Figure 2 shows the measured autocorrelation function, i.e., $\rho(x, z, \tau) \leq \langle u(x, z, t + \tau)u(x, z, t) \rangle_t$, where the first peak corresponds to the turnover time

$\tau_0 \approx 50 \text{ s}$. Therefore, the Bolgiano time scale is around $\tau_B \sim 1 \text{ s}$ and the Kolmogorov time scale is around $\tau_\eta \sim 0.1 \text{ s}$. Hence, the present data does not resolve the Kolmogorov time scale. Note that previous numerical studies have found that energy dissipation rates are spatially inhomogeneous^[26-28]. We do not use the Kolmogorov time scale τ_η to scale the separation τ here due to the lack of measurements of energy dissipation rates. Previously, the horizontal velocity component $u(x, z)$ has been found to obey the K41-like scaling in spatial domain for both near the sidewall and at the cell center^[22]. We note the inertial range in Ref.[22] is quite short. For example, the inertial range in the central region is in the range $0.004 \text{ m}-0.02 \text{ m}$, around 0.7 decade. We argue here that the spatial inhomogeneous effect, especially in the near sidewall region has taken into account.

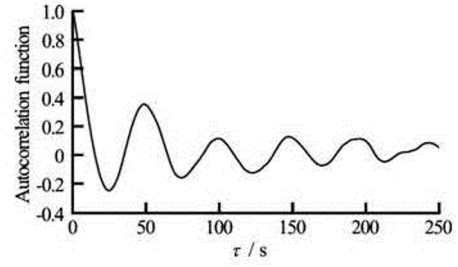


Fig.2 Measured temporal autocorrelation function $\rho(x, z, \tau)$ in the near sidewall region. Graphically, the turnover time (resp. the period of the large-scale circulation) is around $T = 50 \text{ s}$. The global Bolgiano length scale is $L_B \approx 0.005 \text{ m}$, the Kolmogorov length scale is $\eta \approx 0.004 \text{ m}$, and the Taylor's microscale is $\lambda \approx 0.008 \text{ m}$. The corresponding Bolgiano timescale is $\tau_B \sim 1 \text{ s}$, and the Kolmogorov time scale is $\tau_\eta \sim 0.1 \text{ s}$. Note that both the Bolgiano scale and Kolmogorov scale are inhomogeneous in space

2.2 Spatial inhomogeneity of the convection cell

To understand the spatial inhomogeneity, the time average horizontal velocity $U(x, z)|_t$ and the root mean square (rms) velocity $u_{\text{rms}}(x, z)|_t$ are calculated. Figure 3 shows (a) the z -direction average velocity $\langle U(x, z)|_t \rangle_z$ (solid line) and the corresponding rms velocity $\langle u_{\text{rms}}(x, z)|_t \rangle_z$ (dashed line), (b) the corresponding x -direction average. Graphically, both the mean velocity $U(x, z)$ and the rms velocity $u_{\text{rms}}(x, z)$ are strong x -dependent when $x/D < 0.24$, and seems to be homogeneous when $x/D > 0.24$, the central region^[29]. This is consistent with recent study that the effects of buoyant forces are spatially inhomoge-

neous, i.e., buoyancy effects are found to vanish gradually when moving away from the cell sidewall, due to the inhomogeneous distributions of thermal plumes in a closed convection cell^[30]. Based on the Fig.3(a), the measurement region is thus termed into three parts, i.e., 1—the boundary layer $0 < x/D < 0.038$, 2—the near sidewall region $0.038 < x/D < 0.24$, where $U(x, z)|_{t,z} > u_{\text{rms}}(x, z)|_{t,z}$, and 3—the central region $0.24 < x/D < 0.5$, where $U(x, z)|_{t,z} < u_{\text{rms}}(x, z)$, respectively^[29]. Note that the boundary layer is of the Prandtl-Blasius type with a varying thickness in both time and space^[31]. The boundary layer for $0 < x/D < 0.038$ is thus in the statistical sense. Thermal plumes are believed to be abundant in the near sidewall region and are rare in the central region^[29].

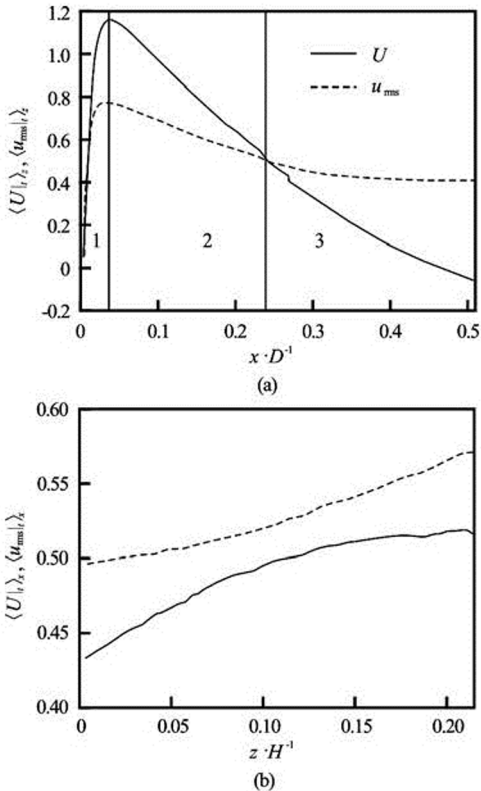


Fig.3 (a) Measured z -direction average horizontal velocity $\langle U(x, z)|_t \rangle_z$ and the rms velocity $\langle u_{\text{rms}}(x, z)|_t \rangle_z$, and (b) the x -direction average $\langle U(x, z)|_t \rangle_x$ and $\langle u_{\text{rms}}(x, z)|_t \rangle_x$. Based on the distance from the wall, the flow is termed into three different regions, i.e., the boundary layer $0 < x/D < 0.038$, the near sidewall region $0.038 < x/D < 0.24$, where $U(x, z)|_z > u_{\text{rms}}(x, z)|_z$, and the central region $0.24 < x/D < 0.5$, where $U(x, z)|_z < u_{\text{rms}}(x, z)|_z$. Note that the thermal plume is abundant in the near sidewall region and is rare in the central region

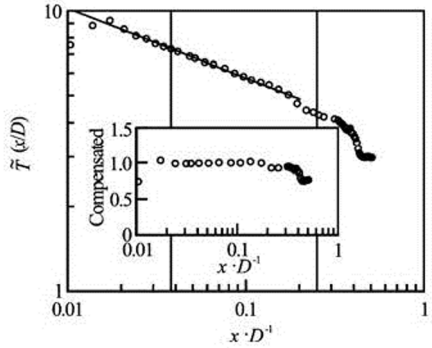


Fig.4 Measured z -direction averaged integral time scale $\tilde{T}(x/D)$ in a log-log plot. The near sidewall range $0.038 < x/D < 0.24$ is illustrated by a vertical solid line. A power law behavior is observed on the range $0.02 < x/D < 0.2$ with a scaling exponent 0.25 ± 0.02 , in which the inset shows the compensated $T(x/D)(x/D)^{1/4} C_T$ with a fitting parameter C_T . Note that the integral time scale is approximately constant, i.e., 3 s, when approaching to the center range $x/D > 0.4$

We now turn to the integral time scale T . The integral time scale is defined as

$$T(x, z) = \int_0^{+\infty} \rho(x, z, \tau) d\tau \quad (11)$$

In practice, the integral time scale T is calculated on the range $0 < \tau < \tau_z$, where τ_z is the location of the first zero-crossing. Again, the measured $T(x, z)$ is a function of x and z , showing a strong x -direction dependence (not shown here). Figure 4 shows a z -direction average integral time scale $\tilde{T}(x/D)$ in a log-log plot. A power law behavior is observed on the range $0.02 < x/D < 0.2$, i.e.,

$$\tilde{T}\left(\frac{x}{D}\right) = C_T \left(\frac{x}{D}\right)^{-\beta} \quad (12)$$

where $C_T = 3.33 \pm 0.05$ and $\beta = 0.25 \pm 0.02$ obtained by using a least square fitting algorithm. The integral time scale T could be interpreted as average time scale in a statistic sense at a given location. The observed power law indicates that the turbulent structures are decreasing with respect to the wall distance x/D . In the cell center \tilde{T} is a constant, i.e., 3 s when approaching to the cell center. This confirms the validation of the spatial homogeneity in this region^[29].

To avoid such inhomogeneous effects and as buoyant forces are exerted on the fluid in the vertical direction, here we consider only the horizontal component of the velocity, $u(x, z)$, in temporal domain.

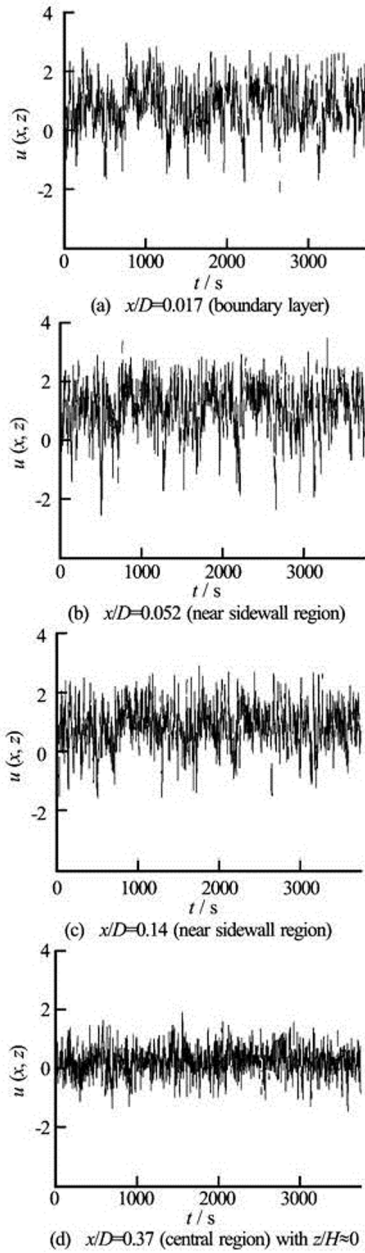


Fig.5 Measured velocity $u(x,z)$ four given locations with $z/H \approx 0$. Visually, they are statistical stationary in temporal domain

Figure 5 shows the horizontal velocity component $u(x,z)$ at several measurement locations. Visually, the velocity $u(x,z)$ is quite stationary in temporal domain at all measurement locations. To relate the scaling behaviors obtained in temporal domain to theoretical predictions in spatial domain, we invoke the elliptic model^[32,33], which was advanced based on a systematic second-order Taylor-series expansion of the space-time velocity correlation functions $C(r, \tau)$. Indeed, several experimental studies in turbulent RB convection have shown that the scaling exponents

measured in temporal domain are the same as those obtained in spatial domain if the elliptic model is invoked^[30,34,35], and some recent Re -measurements were also based on the elliptic model^[36].

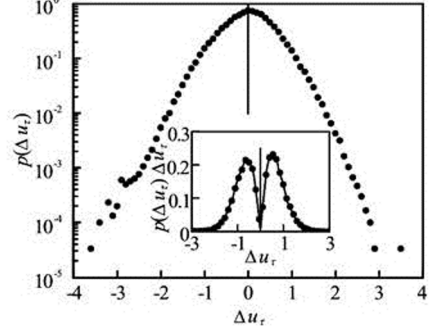


Fig.6 Measured pdf $p(\Delta u_\tau)$ for $u(x,z)$ at location $x/D \approx 0.42$ and $z/H \approx 0.20$ with 5×5 velocity grids and a time separation $\tau = 10$ s, in which the normal distribution is illustrated by a solid line. The inset shows the integral kernel $p(\Delta u_\tau)\Delta u_\tau$ for the first-order structure-function. The location of maximum pdf (illustrated by a vertical line) is around $\Delta u_\tau \approx 0$, indicating that $p_{\max}(\tau)$ almost has no contribution to the first-order structure-function. The pdf scaling of $p_{\max}(\tau)$ thus represents a background fluctuation without the influence of large scale structures, e.g., thermal plumes, large-scale-circulation, etc.

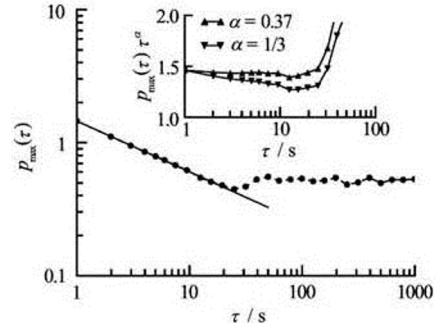


Fig.7 Measured $p_{\max}(\tau)$ for the horizontal velocity $u(x,z)$ at location $x/D = 0.42$ and $z/H = 0.20$ with 10×10 velocity grids. A more than one decade inertial range is observed on the range $1 \text{ s} \leq \tau \leq 20 \text{ s}$ with a scaling exponent $\alpha \approx 0.37$, a scaling exponent reported for the turbulent velocity of high-Reynolds homogeneous and isotropic turbulent flows. The inset shows the compensated $p_{\max}(\tau)\tau^\alpha$ respectively with $\alpha = 1/3$ (downward triangles) and $\alpha = 0.37$ (triangles) to emphasize the power law behavior

3. Results and discussion

3.1 Scaling of probability density function

Figure 6 shows the empirical pdf $p_\tau(\Delta u_\tau)$, for

$u(x, z)$ at the location $x/D \approx 0.42$ and $z/H \approx 0.20$ with 5×5 velocity grids and a time separation $\tau = 10$ s, in which the normal distribution is illustrated by a solid line. The corresponding $\rho_{\max}(\tau)$ is illustrated by a vertical solid line. Note that the location of the maximum pdf $\max_{\Delta u_\tau} p_\tau(\Delta u_\tau)$ is around $\Delta u_\tau \approx 0$ for all separation scales. To compare with the first-order SF, we show the integral kernel $u_\tau p_\tau(\Delta u_\tau)$ as inset. Note that the $\rho_{\max}(\tau)$ almost has no contribution to the SF^[13]. Therefore, the pdf scaling represents a real background fluctuation without the influence of large-scale structures, e.g., thermal plumes, LSC etc.. Figure 7 shows $\rho_{\max}(\tau)$ measured at $x/D = 0.42$ and $z/H = 0.42$, the position close to the cell's central region. To acquire accurate statistics, $\rho_{\max}(\tau)$ was calculated within an area of 0.000066×0.000066 m², i.e., 10×10 velocity vectors, corresponding to 6.4×10^5 ($10 \times 10 \times 7500 \times 0.85$, number of velocity vectors in x -direction \times number of velocity vectors in z -direction \times number of vector maps \times mean ratio of valid velocity vectors) data points. According to Ref.[13], this can provide a quite good estimation of α if there exists any power-law behavior. The inset shows the compensated $\rho_{\max}(\tau)\tau^{-\alpha}$ with $\alpha = 1/3$ and $\alpha = 0.37$. Visually, a quite clean power-law behavior is observed for the range $1 \text{ s} \leq \tau \leq 20 \text{ s}$ with a scaling exponent $\alpha \approx 0.37$. It is interesting to note that the index value of α here is consistent with the first-order SF scaling exponent, $\zeta(1) = 0.37$, reported in other studies for high-Reynolds-number turbulent flows^[3,4,37]. This confirms the pdf scaling for the horizontal velocity and implies, despite of a relatively small Reynolds number, the same intermittent correction as those in high-Reynolds-number turbulent flows.

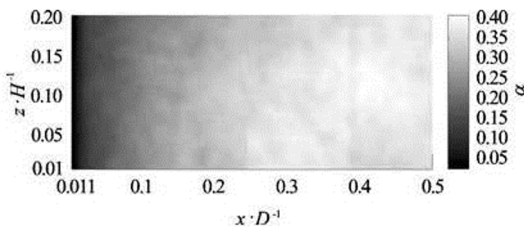


Fig.8 Measured $\alpha(x, z)$ of the horizontal velocity on the measurement domain $0.01 < x/D < 0.5$ and $0.01 < z/H < 0.21$ with a 5×5 spatial velocity grids and 1 moving grid in both x and z directions. It corresponds to 1.6×10^5 data points for each realization. Visually, the measured $\alpha(x, z)$ shows a strong x -dependence

To further evaluate the spatial distribution of $\alpha(x, z)$, $\rho_{\max}(\tau)$ at each position (x, z) was calcu-

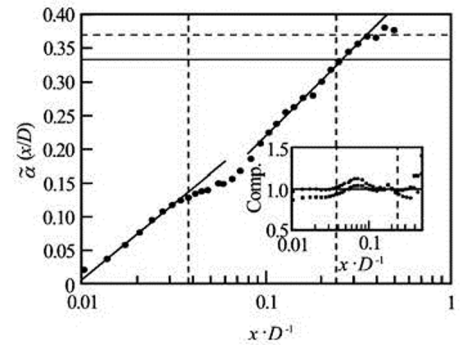


Fig.9 The z -direction spatial averaged scaling exponents $\tilde{\alpha}(x/D)$ in a semilog plot. The index values $1/3$ and 0.37 are illustrated respectively by the horizontal solid line and dashed line. The vertical dashed line indicates the range of the velocity boundary layer, $x/D < 0.038$, the near sidewall range $0.038 < x/D < 0.24$ and the central region $0.24 < x/D$, respectively. Logarithm laws are observed in the range $0.01 < x/D < 0.03$ and $0.1 < x/D < 0.4$ respectively with scaling exponents 0.22 ± 0.02 and 0.28 ± 0.02 . The inset shows the compensated curves to emphasize the observed log laws

lated within an area of 5×5 velocity vectors, corresponding to $25 \times 7500 \times 0.85 = 1.6 \times 10^5$ (number of velocity vectors \times number of vector maps \times mean ratio of valid velocity vectors) data points, which is long enough to provide a good estimation of α ^[13]. We plot the spatial distribution of the estimated $\alpha(x, z)$ in Fig.8, which shows a strong x -dependence. It implies the inhomogeneity in probability space and might be understood as the effect of the sidewall (resp. thermal plumes). On the other hand, the z -dependence of $\alpha(x, z)$ is much weaker. We thus calculate the z -averaged (vertical-direction-averaged) exponent $\tilde{\alpha}(x)$ as

$$\tilde{\alpha}(x) = \langle \alpha(x, z) \rangle_z = \frac{1}{\Delta z} \int \alpha(x, z) dz \quad (13)$$

where $\Delta z = 0.041$ m $\approx 0.2H$. Figure 9 shows the measured $\tilde{\alpha}(x)$ in a semilog plot, in which the index values $1/3$ and 0.37 are illustrated respectively by horizontal solid and dashed lines. Graphically, $\tilde{\alpha}(x)$ reaches the K41 value $1/3$ around $x/D = 0.26$, and arrives 0.37 around $x/D = 0.32$. This further confirms previous findings that in the central region of the cell the velocity field exhibit the same scaling behavior that one would find in homogeneous and isotropic Navier-Stokes turbulence^[22,29,30,38]. Moreover, two logarithm laws are observed in the velocity boundary layer $0.01 < x/D < 0.03$ and $0.1 < x/D < 0.44$ i.e.,

$$\tilde{\alpha}\left(\frac{x}{D}\right) = \xi \log_{10}\left(\frac{x}{D}\right) \quad (14)$$

where ξ are found to be respectively 0.22 ± 0.02 and 0.28 ± 0.02 obtained graphically. To emphasize these observed log-laws, a compensated curve $[\tilde{\alpha}(x/D) - C][\xi \lg_{10}(x/D)]^{-1}$ is shown as inset in Fig.9, in which C is the fitting prefactor. The observed plateau confirms the existence of the log-law. Note that we do not have theory for the wall effect here. More database should be investigated in future to confirm whether these log-law is universal for RB cell.

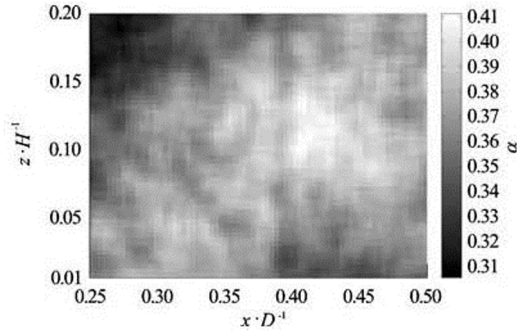


Fig.10 Re-plot measured $\alpha(x,z)$ in the measurement domains $0.25 < x/D < 0.5$ and $0.01 < z/H < 0.21$ with a 5×5 spatial velocity grids and 1 moving velocity grid in both directions. A spatial pattern, fluctuating over the range $0.28 < \alpha < 0.41$, is observed, indicating an inhomogeneous property of the RB convection system even in the cell center

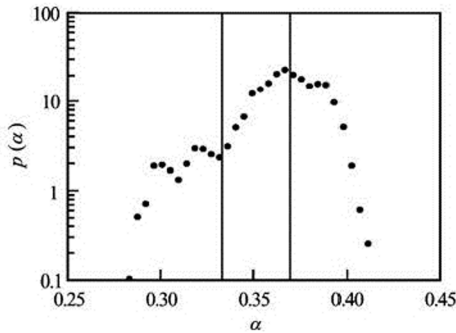


Fig.11 Empirical probability density function of α on the range $0.25 < x/D < 0.5$. The vertical line indicates the value $\alpha = 1/3$ and $\alpha = 0.37$. Note that the most probability value is around 0.37

We are particularly interested in the central region $0.25 < x/D < 0.5$, which is far away from the sidewall and where the wall effects become weaker. We replot the $\alpha(x,z)$ within the range $0.25 < x/D < 0.5$ in Fig.10. It shows a spatial pattern, fluctuating over the range $0.28 < \alpha < 0.41$. We have tested for more

data points by including more velocity grids from 5×5 to 10×10 . This pattern does not change. It is certainly beyond statistical errors and cannot be an artificiality of the scheme we used. The origin of this pattern is unclear. Figure 11 presents the corresponding pdf of α , in which the index values $1/3$ and 0.37 are demonstrated by vertical solid lines. One can find that the distribution deviates obviously from a Gaussian distribution. The most probability value is about 0.37 , the value of the first-order SF for high-Reynolds number turbulent flows. We have $\langle \alpha(x,z) \rangle|_{x,z} = 0.36 \pm 0.02$.

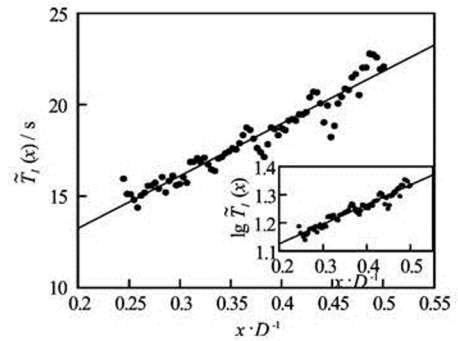


Fig.12 The z -direction averaged length of the power law range $\tilde{T}_l(x/D)$ in linear-linear plot, in which the solid line is a linear fitting with a slope $\phi = 28.6 \pm 1.9$. The inset shows the time length of the measured $\tilde{T}_l(x/D)$ in decades, in which the solid line is a least square fitting with a slope 0.69 ± 0.05 . Note that the measured $\tilde{T}_l(x/D)$ strongly depends on the wall distance x/D

We denote here T_l as the time length of the inertial range for $p_{\max}(\tau)$, i.e.,

$$T_l = \tau_E - \tau_S \quad (15)$$

where τ_S is the lower end of the inertial range, i.e., 1 s, and τ_E is the end of the inertial range. The measured T_l is showing x -dependent (not shown here). Note that in the present case, we do not have the resolution of the Kolmogorov scale, which is in the order -0.1 s. Therefore, if we take the 1 s as the lower end τ_S of the inertial range, then the corresponding length of the inertial range is at least 1.0-1.4 decades in the logarithm frame, i.e., $T_l = \lg_{10}(\tau_E) - \lg_{10}(\tau_S)$. This inertial range is significant larger than the one reported in Ref.[22], in which an inertial range is typically found to be $0.004 \text{ m} < r < 0.02 \text{ m}$, corresponding to 0.7 decade, in spatial domain in the central region of the cell. The reason for the different length of the inertial range in the spatial and temporal domains might be the effect of the spatial inhomogeneity of the turbulent flow

in RB cell as we emphasized previously, see Figs.3 and 10. Figure 12 displays the z -direction averaged $\tilde{T}_l(x/D)$, in which the inset shows the corresponding length in decades $\tilde{T}_l(x/D)$. Graphically, it suggests a linear relation

$$\tilde{T}_l\left(\frac{x}{D}\right) \sim \frac{\phi x}{D} \quad (16)$$

with the slope $\phi = 28.6 \pm 1.9$. For the measured T_l , a linear relation is found to be, i.e.,

$$\tilde{T}_l\left(\frac{x}{D}\right) \sim \frac{\varphi x}{D} \quad (17)$$

with the slope $\varphi = 0.69 \pm 0.05$. We understand these wall-dependent relations as the effect of both wall boundary and thermal plumes, which is also associated with the near sidewall region.

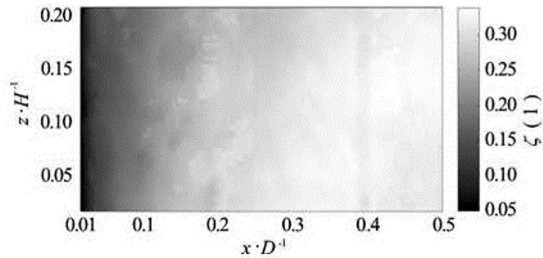


Fig.13 Measured first-order SF scaling exponent $\zeta(1,x,z)$ by using the same moving-grid algorithm for the pdf scaling. Note that the measured $\zeta(1,x,z)$ also shows x -dependence

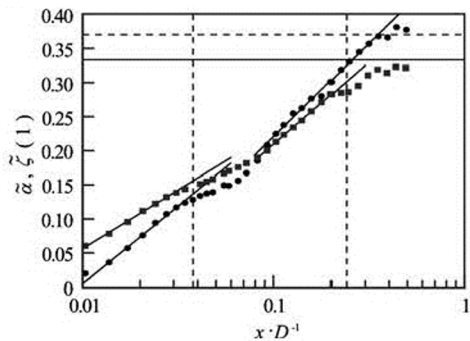


Fig.14 The z -direction averaged $\zeta(1,x)$ (squares) in a semi-log plot, in which the index values $1/3$ (solid line) and 0.37 (dashed line) are also shown. The vertical dashed line indicates the range of the velocity boundary layer, $x/D < 0.038$, the near sidewall range $0.038 < x/D < 0.24$ and the central region $0.24 < x/D$, respectively. Logarithm law is observed in the velocity boundary layer with a scaling exponent 0.17 ± 0.22 and on the range $0.1 < x/D < 0.2$ with a scaling exponent 0.24 ± 0.02 , respectively. For comparison, the measured $\tilde{\alpha}$ is also replotted (circles)

3.2 First-order structure function: A comparison

For comparison, we perform the same algorithm for the first-order SF in temporal domain. Figure 13 shows the measured scaling exponent $\zeta(1,x,z)$ for the first-order SF. Graphically, it is also x -dependent, especially on the near sidewall region. This is consistent with Fig.8. The fluctuation range of the scaling exponent α is larger than $\zeta(1)$. Figure 14 shows the z -direction averaged $\tilde{\zeta}(1,x/D)$, in which the solid line is the logarithm fitting respectively with scaling exponent 0.17 ± 0.02 and 0.24 ± 0.02 . It is close to the K41 value when $x/D > 0.2$. We could term the measured $\tilde{\zeta}(1,x/D)$ into two regimes. The first regime is on the range $0.01 < x/D < 0.1$, where $\zeta(1,x/D) > \tilde{\alpha}(x/D)$. The second one is $x/D > 0.1$, in which $\zeta(1,x/D) < \tilde{\alpha}(x/D)$. Figure 15 reproduces the measured $\zeta(1,x,z)$ in the range $0.25 < x < 0.5$. Visually, it seems that, despite of a small value, the measured $\zeta(1)$ is a smooth version of α . However, both the first-order SF scaling $\zeta(1)$ and the pdf scaling α show a similar spatial pattern and wall dependence.

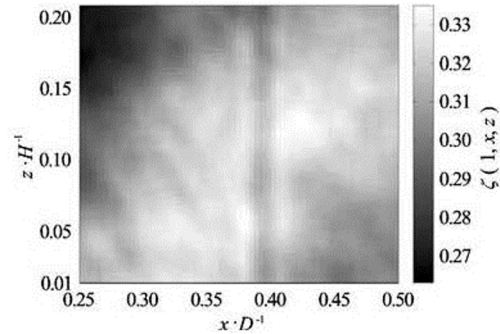


Fig.15 Replot the measured $\zeta(1,x,z)$ in the range $0.25 < x/D < 0.50$, which fluctuates in the range of $0.26 < \zeta(1) < 0.33$. A similar spatial pattern as shown in Fig.10 is observed. Note that the pattern provided by SF can be seen as a smooth version of the one provided by the pdf

3.3 He's Elliptic model

As we mentioned above that to convert the temporal domain to spatial domain, Taylor's frozen hypothesis is usually applied^[21]. However, in RB cell, conditions for Taylor's hypothesis are not satisfied^[39]. Note that Taylor's frozen hypothesis is the first-order expansion of the correlation function in which only the mean convection velocity is involved^[32]. More recently, He and Zhang^[32] proposed a second-order expansion theory to convert the measurement from the temporal domain to spatial domain. This second-order formula is named as elliptic model, i.e.,

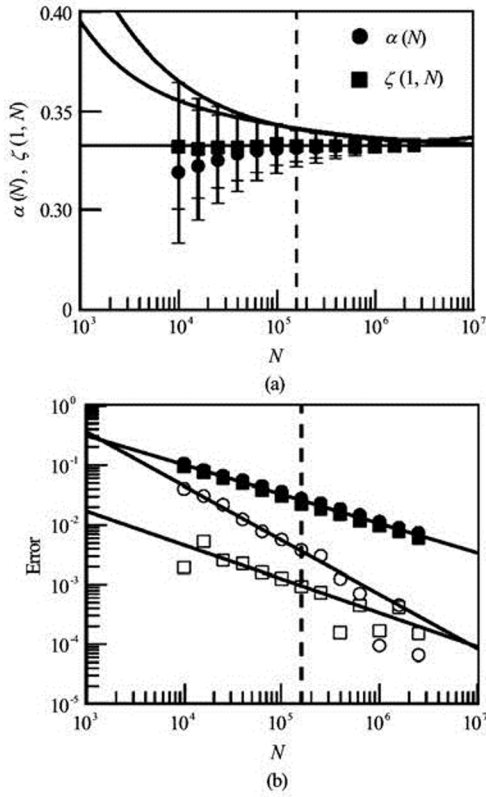


Fig.16 A statistics test of the length dependent $\alpha(N)$ and $\zeta(1, N)$ (circles) for the Hurst number $H = 1/3$ with 1 000 realizations for each fBm simulation with various N in data points. (a) The measured scaling exponents $\alpha(N)$ (circles) and $\zeta(1, N)$ (squares). The error bar is the standard deviation of the measured scaling exponent from the 1 000 realizations. The solid line is a power law fitting of the error bar. (b) The corresponding error-bar (closed symbols) and relative error $Er(N) = [H - \zeta(1, N)]/H$ (open symbols). The solid line is the power law fitting with scaling an exponent 0.50 ± 0.02 for the measured errorbar and the relative error for the first-order SF, and an scaling exponent 0.91 ± 0.02 for the relative error for the pdf scaling, respectively. Note that when $N > 10^5$, the first-order SF provides a relative error less than 0.1% and a standard deviation less than 3%. The vertical dashed line indicates the validation data length from PIV measurement

$$r_E^2 = (r - U_0\tau)^2 + V^2\tau^2 \quad (18)$$

in which U_0 is a characteristic convection velocity proportional to the mean velocity U , and V is the sweeping velocity associated with the rms. velocity and the shear-induced velocity^[32]. The validation of He's model in RB cell has been verified experimentally in several works^[34,36,40]. However, Zhou et al.^[40] found that the convection velocity U_0 and sweeping velocity V are indeed have spatial distribution. It is

not easy to relate our temporal scaling exponents $\zeta(1)$ and α with the spatial domain ones since the flow here is spatial inhomogeneous. Therefore, one cannot perform one to one comparison between the present results with the ones reported in Ref.[22].

3.4 Finite size effect of data sample

To exclude the effect of finite sample size, we perform a fractional Brownian motion (fBm) simulation with a Hurst number $H = 1/3$. fBm simulation was realized by using a Wood-Chan algorithm^[41] with 1 000 realizations and various data length N . We chose the data length $10^4 < N < 3.2 \times 10^6$. The scaling exponent of the first-order SF $\zeta(1, N)$ is then estimated on the range $10 < \tau < 1000$ data points. Figure 16 shows the measured $\zeta(1, N)$, in which the errorbar was the standard deviation of the estimated $\zeta(1, N)$ from 1 000 realizations. The solid line is power law fitting of the error-bar. Note that the estimated $\zeta(1, N)$ is asymptotic to the given H very quickly. The inset shows an relative of the estimated $\zeta(1, N)$, i.e., $Er(N) = [H - \zeta(1, N)]/H$ (circles), and $\delta\zeta(1, N)/H$ (squares), respectively. The solid lines are power law fitting with slope 0.50 ± 0.02 for the error-bars and the relative error for the first-order SF, and 0.09 ± 0.02 for the relative error of pdf scaling, respectively. The former slope 0.5 is consistent with the previously finding for the pdf scaling^[13]. Note that when $N > 10^5$, the first-order SF provides a relative error less than 0.1% and a standard deviation less than 3%. In the present study, the data length is about 1.6×10^5 , which provides a quite good statistical convergence for both the first-order SF and the pdf scaling. Therefore, the experimental results reported here cannot be the finite size sample effect.

4. Conclusions

In summary, in this study, we have extended our previous work^[13] and generalized the pdf scaling analysis to turbulent velocity in turbulent RB convection cell. The integral time scale is found to obey a power law in the range $0.02 < x/D < 0.2$ with a scaling exponent 0.25 ± 0.02 . We confirmed the pdf scaling for the horizontal velocity in probability space. The estimated $\alpha(x, z)$ is strongly inhomogeneous with respect to the x -direction and the z -dependence of $\alpha(x, z)$ is much weaker, which can be understood as the effect of the sidewall. The scaling exponent $\alpha(x, z)$ shows its own spatial pattern. Moreover, the z -direction-averaged $\tilde{\alpha}(x)$ obeys a logarithm law with respect to x , the distance from the sidewall, with a sca-

ling exponent $\beta = 0.22 \pm 0.02$ in the velocity boundary layer, i.e., $x/D < 0.03$, and $\beta = 0.28 \pm 0.02$ on the range $0.1 < x/D < 0.4$, respectively. In the cell's central region, the $\alpha(x, z)$ fluctuates around 0.37. Despite of the quite low Reynolds number here, the scaling exponent $\alpha = 0.36 \pm 0.02$ is consistent with the first-order SFs scaling exponent $\zeta(1)$ for high-Reynolds-number turbulent flows reported in other studies. It is interesting to note that the pdf itself has almost the same intermittent correction as the first-order SFs scaling in high-Reynolds-number turbulent flows. Furthermore, the z -direction averaged length of the inertial range $\tilde{T}_I(x)$ is increasing linearly with the distance from the wall. Equivalently, the measured length of the inertial range represented in decade $\tilde{T}_I(x)$ is linear increasing with x/D with a slope 0.69 ± 0.05 . Finally, the pdf scaling analysis is compared with the first-order SF. The experimental results show similar spatial pattern for both α and $\zeta(1)$, and also similar wall-dependence of z -direction averaged $\tilde{\alpha}(x/D)$ and $\tilde{\zeta}(1, x/D)$. Note that the numerical difference between the measured α and $\zeta(1)$ is from the fact that the pdf scaling reflect the background fluctuations, while the first-order SF takes all the turbulent structures into account, including the thermal plumes, LSC, etc..

References

- [1] KOLMOGOROV A. N. Local structure of turbulence in an incompressible fluid at very high Reynolds numbers[J]. *Doklady Akademii Nauk SSSR*, 1941, 30(4): 301-305.
- [2] FRISCH U. *Turbulence: The legacy of AN Kolmogorov*[M]. Cambridge, UK: Cambridge University Press, 1995.
- [3] SHE Z. S., LEVEQUE E. Universal scaling laws in fully developed turbulence[J]. *Physical Review Letter*, 1994, 72(3): 336-339.
- [4] ARNEODO A., BAUDET C. and BENZI R. et al. Structure functions in turbulence, in various flow configurations, at Reynolds number between 30 and 5000, using extended self-similarity[J]. *Europhysics Letters*, 1996, 34(6): 411-416.
- [5] SREENIVASAN K., ANTONIA R. The phenomenology of small-scale turbulence[J]. *Annual Review Fluid Mechanics*, 1997, 39: 435-472.
- [6] LOHSE D., XIA K. Q. Small-scale properties of turbulent Rayleigh-Benard convection[J]. *Annual Review Fluid Mechanics*, 2010, 42: 335-364.
- [7] LASHERMES B., ROUX S. and ABRY P. Comprehensive multifractal analysis of turbulent velocity using the wavelet leaders[J]. *European Physical Journal B*, 2008, 61(2): 201-215.
- [8] KOWAL G., LAZARIAN A. Velocity field of compressible magnetohydrodynamic turbulence: Wavelet decomposition and mode scalings[J]. *Astrophysics Journal*, 2010, 720: 742-756.
- [9] LORD J. W., RAST M. P. and MCKINLAY C. et al. Wavelet decomposition of forced turbulence: Applicability of the iterative Donoho-Johnstone threshold[J]. *Physics of Fluids*, 2012, 24(2): 025102.
- [10] HUANG Y. X., SCHMITT F. G. and LU Z. M. et al., An amplitude-frequency study of turbulent scaling intermittency using Hilbert spectral analysis[J]. *Europhysics Letters*, 2008, 84(4): 40010.
- [11] HUANG Y. X. Arbitrary-order hilbert spectral analysis: Definition and application to fully developed turbulence and environmental time series[D]. Doctoral Thesis, Lille, France: University des Sciences et Technologies de Lille and Shanghai, China: Shanghai University, 2009.
- [12] HUANG Y. X., SCHMITT F. G. and HERMAND J. P. et al. Arbitrary-order Hilbert spectral analysis for time series possessing scaling statistics: Comparison study with detrended fluctuation analysis and wavelet leaders[J]. *Physical Review E*, 2011, 84(1): 016208.
- [13] HUANG Y. X., SCHMITT F. G. and ZHOU Q. et al., Scaling of maximum probability density functions of velocity and temperature increments in turbulent systems[J]. *Physical of Fluids*, 2011, 23(12): 125101.
- [14] DAVIDSON P. A., PEARSON B. R. Identifying turbulent energy distribution in real, rather than fourier, space[J]. *Physical Review Letters*, 2005, 95(21): 214501.
- [15] HUANG Y. X., SCHMITT F. G. and LU Z. M. et al., Analysis of daily river flow fluctuations using empirical mode decomposition and arbitrary order Hilbert spectral analysis[J]. *Journal of Hydrology*, 2009, 373(1-2): 103-111.
- [16] HUANG Y. X., SCHMITT F. G. and LU Z. M. et al.. Second-order structure function in fully developed turbulence[J]. *Physical Review E*, 2010, 82(2): 26319.
- [17] HUANG Y. X., BIFERALE L. and CALZAVARINI E. et al. Lagrangian single particle turbulent statistics through the Hilbert-Huang transforms[J]. *Physical Review E*, 2013, 87(4): 041003.
- [18] HUANG N. E., SHEN Z. and LONG S. R. A new view of nonlinear water waves: The hilbert spectrum[J]. *Annual Review of Fluid Mechanics*, 1999, 31: 417-457.
- [19] BOLGIANO R. Turbulent spectra in a stably stratified atmosphere[J]. *Journal of Geophysical Research*, 1959, 64(12): 2226-2229.
- [20] OBUKHOV A. M. On the influence of archimedean forces on the structure of the temperature led in a turbulent flow[J]. *Doklady Akademii Nauk SSSR*, 1959, 125: 1246-1248.
- [21] AHLERS G., GROSSMANN S. and LOHSE D. Heat transfer and large scale dynamics in turbulent Rayleigh-Benard convection[J]. *Review of Modern Physics*, 2009, 81(2): 503-537.
- [22] SUN C., ZHOU Q. and XIA K. Q. Cascades of velocity and temperature fluctuations in buoyancy-driven turbulence[J]. *Physical Review Letters*, 2006, 97(14): 144504.
- [23] ZHOU Q., SUN C. and XIA K. Q. Experimental investigation of homogeneity, isotropy, and circulation of the velocity field in buoyancy-driven turbulence[J]. *Journal of Fluid Mechanics*, 2008, 598: 361-372.
- [24] GASTEUIL Y., SHEW W. and GILBERT M. et al., Lagrangian temperature, velocity, and local heat flux measurement in Rayleigh-Benard convection[J]. *Physical Review Letters*, 2007, 99(23): 234302.

- [25] GROSSMANN S., LOHSE D. Fluctuations in turbulent Rayleigh-Benard convection: The role of plumes[J]. **Physics of Fluids**, 2004, 16(12): 4462-4472.
- [26] BENZI R., TOSCHI F. and TRIPICCIONE R. On the heat transfer in Rayleigh-Benard systems[J]. **Journal of Statistical Physics**, 1998, 93(8): 901-918.
- [27] CALZAVARINI E., TOSCHI F. and TRIPICCIONE R. Evidences of bolgiano-obhukhov scaling in three-dimensional Rayleigh-Benard convection[J]. **Physical Review E**, 2002, 66(1): 016304.
- [28] KUNNEN R., CLERCX H. and GEURTS B. et al. Numerical and experimental investigation of structure-function scaling in turbulent Rayleigh-Benard convection[J]. **Physical Review E**, 2008, 77(1): 016302.
- [29] ZHOU Q., XIA K. Q. Comparative experimental study of local mixing of active and passive scalars in turbulent thermal convection[J]. **Physical Review E**, 2008, 77(5): 056312.
- [30] ZHOU Q., XIA K. Q. Disentangle plume-induced anisotropy in the velocity field in buoyancy-driven turbulence[J]. **Journal of Fluid Mechanics**, 2011, 684: 192-203.
- [31] ZHOU Q., XIA K. Q. Measured instantaneous viscous boundary layer in turbulent Rayleigh-Benard convection[J]. **Physical Review Letters**, 2010, 104(10): 104301.
- [32] HE G. W., ZHANG J. B. Elliptic model for space-time correlations in turbulent shear flows[J]. **Physical Review E**, 2006, 73(5): 055303(R).
- [33] ZHAO X., HE G. W. Space-time correlations of fluctuating velocities in turbulent shear flows[J]. **Physical Review E**, 2009, 79(2): 046316.
- [34] HE X. Z., HE G. W. and TONG P. Small-scale turbulent fluctuations beyond Taylor's frozen-flow hypothesis[J]. **Physical Review E**, 2010, 81(6-2): 065303(R).
- [35] HE X. Z., TONG P. Kraichnan's random sweeping hypothesis in homogeneous turbulent convection[J]. **Physical Review E**, 2011, 83(3-2): 037302.
- [36] HE X. Z., FUNFSCHILLING D. and NOBACH H. et al. Transition to the ultimate state of turbulent Rayleigh-Benard convection[J]. **Physical Review Letters**, 2012, 108(2): 024502.
- [37] BENZI R., CILIBERTO S. and TRIPICCIONE R. et al. Extended self-similarity in turbulent flows[J]. **Physical Review E**, 1993, 48(1): 29-32.
- [38] NI R., HUANG S. D. and XIA K. Q. Local energy dissipation rate balances local heat flux in the center of turbulent thermal convection[J]. **Physical Review Letters**, 2011, 107(17): 174503.
- [39] SHANG X. D., XIA K. Q. Scaling of the velocity power spectra in turbulent thermal convection[J]. **Physical Review E**, 2001, 64(6): 065301.
- [40] ZHOU Q., LI C. M. and LU Z. M. et al. Experimental investigation of longitudinal space-time correlations of the velocity field in turbulent Rayleigh-Benard convection[J]. **Journal of Fluid Mechanics**, 2011, 683: 94-111.
- [41] WOOD A., CHAN G. Simulation of stationary Gaussian processes in $[0, 1]^d$ [J]. **Journal of Computational and Graphical Statistics**, 1994, 3(4): 409-432.